

Five Stellar Populations in M22 (NGC 6656)

JAE-WOO LEE¹

¹*Department of Physics and Astronomy, Sejong University
209 Neungdong-ro, Gwangjin-Gu, Seoul, 05006, Korea
jaewoolee@sejong.ac.kr; jaewoolee@sejong.edu*

ABSTRACT

We present the Ca–CN–CH photometry of the metal-complex globular cluster (GC) M22 (NGC 6656). Our photometry clearly shows the discrete double CN–CH anticorrelations in M22 red giant branch (RGB) stars, due to the difference in the mean metallicity. The populational number ratio between the two main groups is $n(\text{G1}):n(\text{G2}) = 63:37(\pm 3)$, with the G1 being more metal-poor. Furthermore, the G1 can be divided into two subpopulations with the number ratio of $n(\text{CN-w}):n(\text{CN-s}) = 51:49 (\pm 4)$, while the G2 can be divided into three subpopulations with $n(\text{CN-w}):n(\text{CN-i}):n(\text{CN-s}) = 24:32:44 (\pm 5)$. The proper motion of individual stars in the cluster shows an evidence of internal rotation, showing the G2 with a faster rotation, confirming our previous results from radial velocities. The cumulative radial distributions (CRDs) of individual subpopulations are intriguing in the following aspects: (1) In both main groups, the CRDs of the CN-s subpopulations are more centrally concentrated than other subpopulations. (2) The CRDs of the the G1 CN-s and the G2 CN-s are very similar. (3) Likewise, the G1 CN-w and the G2 CN-w and CN-i have almost identical CRDs. We also estimate the relative helium abundance of individual subpopulations by comparing their RGB bump magnitudes, finding that no helium abundance variation can be seen in the G1, while significant helium enhancements by $\Delta Y \approx 0.03 - 0.07$ are required in the G2. Our results support the idea that M22 formed via a merger of two GCs.

Keywords: Hertzsprung Russell diagram; Globular star clusters; Stellar abundances; Stellar evolution;

1. INTRODUCTION

M22 (NGC 6656) is a metal-complex globular cluster (GC) in our Galaxy and its chemical peculiarity has been known for more than four decades. Hesser & Harris (1979) noticed that M22 appears to have anomalies in its elemental abundances similar to ω Cen. Later, Norris & Freeman (1983) reported the variation in the calcium abundance by up to $\Delta[\text{Ca}/\text{Fe}] \approx 0.3$ dex, which was confirmed later by Marino et al. (2009, 2011) and Lee et al. (2009).

The previous high-resolution spectroscopic studies clearly showed that M22 has a discrete bimodal metallicity distribution and it is an exemplar metal-complex GC¹ (Marino et al. 2009, 2011; Lee 2016). In addition, Lim et al. (2015) reported the double CN–CH anticorrelations in M22 red giant branch (RGB) stars, which was lucidly interpreted by Lee (2015) that they are natural consequences of the bimodal metallicity distribution.

¹ Mucciarelli et al. (2015) argued that RGB stars in M22 do not show any metallicity spread by reanalyzing the data presented by Marino et al. (2011). As we showed in our previous work (Lee 2016), several independent results from not only high- and low-resolution spectroscopy but also narrow and intermediate band photometry show strong evidence of metallicity spread in M22.

From a photometric perspective, two or three groups of stars are classified in M22: Marino et al. (2009) identified the double sub-giant branch using the *HST* F606W/F814W photometry of the cluster. However, they did not list the populational number ratio. Lee et al. (2009) and Lee (2015) employed the *hk* photometry and they showed the discrete double RGB sequences due to the bimodal metallicity distribution. Later, Milone et al. (2017) showed that M22 contains at least three different groups of stars based on the so-called chromosome map (see their Figure 6).

During the past decade, we developed a new set of narrowband photometric systems in order to investigate multiple populations (MPs) in GC RGB and asymptotic giant branch (AGB) stars with small aperture telescopes (Lee 2015, 2017, 2018, 2019a,b). As we elaborately showed, our new photometric system allows us to measure accurate CN, CH, and calcium abundances even in the extremely crowded fields, such as the central part of GCs, where the traditional spectroscopic observations cannot be performed. It is a well-known fact that the nitrogen and carbon abundances can be altered through the CN cycle that occurred in the previous generation of stars, and the existence of the CN–CH anticorrelation indicates the presence of MPs in normal GCs. On the other hand, our photometric calcium abundance can tell the difference in

metallicity among different populations. Consequently, our new photometric system is highly suitable for the study of MPs not only in normal GCs but also in metal-complex GCs.

In this Letter, we investigate the photometric CN–CH anti-correlations in M22, finding five MPs. As we will show later, our new discovery on the cumulative radial distributions (CRDs), helium contents, and kinematical differences between individual populations strengthens our idea that M22 formed via a merger of two GCs (Lee 2015).

2. OBSERVATIONS

The journal of observations of the Ca_{JWL} by photometry is given in Lee (2015). In addition, we also obtained the $JWL39$ photometry using the CTIO 1 m telescope in three separate runs from 2013 April to 2014 May, and the $JWL43$ photometry using the KPNO 0.9 m telescope in two separate runs from May and September in 2018. The updated total integration times for our observations are given in Table 1.

The detailed discussion for our new filter system can be found in Lee (2015, 2017, 2019a,b). The CTIO 1.0 m telescope was equipped with an STA $4k \times 4k$ CCD camera, providing a plate scale of $0''.289 \text{ pixel}^{-1}$ and a field of view (FOV) of $20' \times 20'$. We obtained the photometry for the Strömgren $uvby$, Ca_{CTIO} , Ca_{JWL} , and $JWL39$ using the CTIO 1.0m telescope with the mean airmass of 1.068 ± 0.072 , and the combined FOV of our mosaicked science frames from CTIO runs was $1^\circ \times 1^\circ$. The KPNO 0.9 m telescope was equipped with the Half Degree Imager (HDI), providing a plate scale of $0''.43 \text{ pixel}^{-1}$ and a FOV of $30' \times 30'$, and we obtained Strömgren by and $JWL43$ using the KPNO 0.9m telescope. Since the altitude of M22 from KPNO is very low, with the maximum altitude of about 34° , we paid special attention to acquire the correct extinction coefficients for each filter. The range of airmasses of the photometric standards for the Strömgren by and $JWL43$ filters was from 1.026 to 1.764 for the 2018 May run, and from 1.029 to 1.846 for the 2018 September run. For our M22 field, the range of airmass was from 1.780 to 1.819, similar to the maximum airmasses of the photometric standards. Also, due to the narrow bandwidth of our $JWL43$ filter, the color dependency of the extinction coefficient is negligibly small. Therefore, it is believed that our ch_{JWL} measurements are correct.

The raw data handling was described in detail in our previous works (Lee 2015; Lee & Pogue 2016; Lee 2017). The photometry of M22 and standard stars were analyzed using DAOPHOTII, DAOGROW, ALLSTAR and ALLFRAME, and COLLECT-CCDAVE-NEWTRIAL packages (Stetson 1987, 1994; Lee & Carney 1999).

Finally, we derived the astrometric solutions for individual stars using the data extracted from the Naval Observatory Merged Astrometric Dataset (Zacharias et al. 2004) and the IRAF IMCOORS package.

Table 1. Integration times (s) for M22

New Filters				
y	b	Ca_{JWL}	$JWL39$	$JWL43$
14705	32095	126740	25950	9650

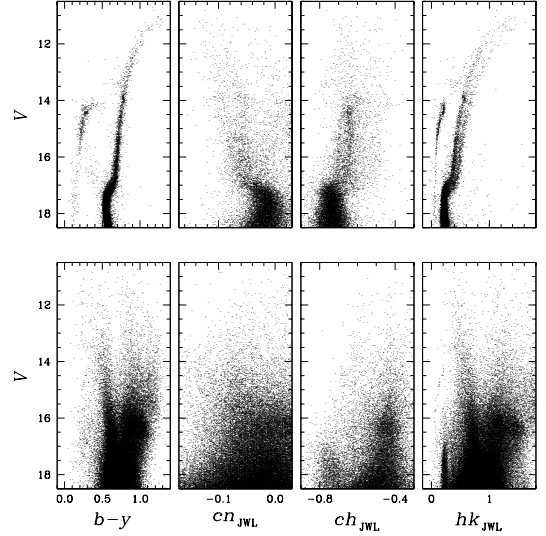


Figure 1. (Top panels) CMDs of M22 membership stars based on the proper motion study of the *Gaia* DR2. A weak bimodal RGB sequence can be seen in the M22 cn_{JWL} CMD, while a broad RGB sequence can be seen in the ch_{JWL} CMD. (Bottom panels) CMDs of the off-cluster field stars.

3. RESULTS

3.1. Color–Magnitude Diagrams

In Figure 1, we show color–magnitude diagrams (CMDs) of bright stars in the M22 field (see also Lee 2015). Using the second *Gaia* date release (*Gaia* DR2; Brown et al. 2018) and our multicolor photometry (see, e.g., Lee 2015), we removed the off-cluster field stars and selected M22 membership RGB stars (e.g., see Milone et al. 2018; Lee 2019b).

Same as our previous work (Lee 2019b), the definitions of photometric indices used in this work are

$$cn_{JWL} = JWL39 - Ca_{JWL}, \quad (1)$$

$$ch_{JWL} = (JWL43 - b) - (b - y). \quad (2)$$

The cn_{JWL} and ch_{JWL} were introduced by the author of the paper and they are excellent photometric measures of the CN band at $\lambda 3883$ and CH G band at $\lambda 4250$, respectively, for cool stars (Lee 2017, 2018, 2019a,b). We note that color excesses of our indices are relatively small, $E(cn_{JWL}) = 0.046 \times E(B - V)$ and $E(ch_{JWL}) = -0.418 \times E(B - V)$, calculated using the method described by Lee et al. (2001), which

Table 2. Populational number ratios (%)

	G1		G2		
	CN-w	CN-s	CN-w	CN-i	CN-s
All	32.4	30.9	8.7	12.0	16.0
G1 only	51.2	48.8
G2 only	23.8	32.6	43.6

Table 3. p -values (%) for Two Sample t -tests for G2 Subpopulations

	G2 CN-i	G2 CN-s
G2 CN-w	0.00	0.00
G2 CN-i		0.35

make our indices less sensitive to variation in foreground reddening. For example, we estimated the degree of variation in foreground reddening of M22 by calculating the $(b-y)$ widths of RGB stars in each group (see below for the definition of the two RGB groups), obtaining $\sigma E(B-V) \approx 0.030$ mag, which results in $\sigma E(cn_{JWL}) \approx 0.001$ mag and $\sigma E(ch_{JWL}) \approx -0.013$ mag, values too negligibly small to affect our results presented in this work.

The RGB sequences were parallelized using the following relation (also see Milone et al. 2017; Lee 2019a,b),

$$\|CI(x) \equiv \frac{CI(x) - CI_{\text{red}}}{CI_{\text{red}} - CI_{\text{blue}}}, \quad (3)$$

where $CI(x)$ is the color index of individual stars and CI_{red} , CI_{blue} are color indices for the fiducials of the red and blue sequences of individual color indices.

3.2. Populational Tagging from the $\|cn_{JWL}$ versus $\|ch_{JWL}$

In our previous studies (e.g., see Lee et al. 2009; Lee 2015), we reported the bimodal calcium distribution of M22 RGB stars (namely, the Ca-w and Ca-s groups) based on their photometric calcium abundances in the Δhk versus V CMD (see the top rightmost panel of Figure 1), which is consistent with high-resolution spectroscopic studies showing the bimodal metallicity distribution of M22 (Marino et al. 2009, 2011; Lee 2016).

In our current study, we perform populational tagging on the $\|cn_{JWL}$ versus $\|ch_{JWL}$ plane. In Figure 2, we show the plot of the $\|cn_{JWL}$ versus $\|ch_{JWL}$ of the M22 RGB stars with $V - V_{\text{HB}} \leq 2.5$ mag. At first glance, two main groups of stars with their own photometric CN-CH anticorrelations can be seen, similar to what can be found in the low-resolution spec-

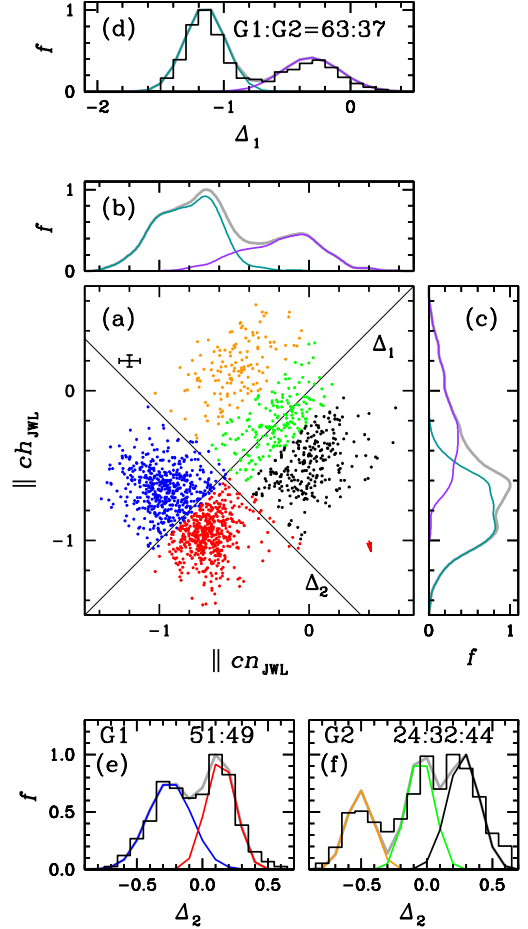


Figure 2. (a) Plot of the $\|cn_{JWL}$ versus $\|ch_{JWL}$ of M22 RGB stars with $V - V_{\text{HB}} \leq 2.5$ mag. The Δ_1 indicates the axis where the decomposition of the main groups, the G1 and G2, is performed. On the other hand, the Δ_2 indicates the axis where decompositions of the subpopulations of the G1 and G2 are performed. The mean measurement errors are also given with black error bars. We also show the differential reddening vector with $E(B-V) = 0.030$ mag is shown with a red arrow, negligibly small to affect our results. (b) The $\|cn_{JWL}$ distributions of the RGB stars. The dark green and purple colors indicate the G1 and G2 populations. Unlike the normal GCs without metallicity spread, such as M5 and NGC 6752, discrete separations in individual populations cannot be seen. (c) Same as (b), but for the $\|ch_{JWL}$ distribution. (d) The Δ_1 distribution. The dark green and purple colors are for the G1 and G2 populations, respectively. The discrete double RGB subpopulations between the G1 and G2 populations can be seen with the number ratio of $n(\text{G1}):n(\text{G2}) = 63:37$. (e) The Δ_2 distribution of the G1 population. The two components can be seen with the number ratio of $n(\text{CN-w}):n(\text{CN-s}) = 51:49$. (f) The Δ_2 distribution of the G2 population. The Gaussian decomposition with three components can reasonably reproduce the observed distribution with the $n(\text{CN-w}):n(\text{CN-i}):n(\text{CN-s}) = 24:32:44$.

troscopic study of the cluster (Lim et al. 2015). As we already discussed in detail (Lee 2015), the difference in the mean metallicity of the two main groups of stars is mainly responsible for these two separate CN–CH anticorrelations in M22: a group of RGB stars with low $\|cn_{JWL}$ and $\|ch_{JWL}$ values is the lower-metallicity population (G1: the blue and red dots in Figure 2 and the definition will be given below), while that with large $\|cn_{JWL}$ and $\|ch_{JWL}$ corresponds to the higher-metallicity population (G2: the black, green, and orange dots). We emphasize that, due to the presence of the multiple subpopulations in M22, and how they lie in this diagram, as well as photometric errors, clear populational separations in the $\|cn_{JWL}$ and $\|ch_{JWL}$ distributions cannot be seen as shown in Figure 2 (b-c).

In order to derive the two main groups of stars, we calculated the RGB distribution projected onto the Δ_1 axis, which is a slope of 1, and we show our result in Figure 2(d). The Δ_1 distribution of RGB stars shows a well-separated bimodal distribution. We employed the expectation maximization (EM) algorithm for the multiple-component Gaussian mixture distribution model to perform the populational tagging. We calculated the probability of individual RGB stars for being the G1 (i.e., RGB stars with smaller Δ_1 values) and G2 (i.e., RGB stars with larger Δ_1 values) groups in an iterative manner, where stars with $P(G1|x_i) \geq 0.5$ from the EM estimator are denoted with the solid dark green lines, which corresponds to the G1 population, while $P(G2|x_i) > 0.5$ with the solid purple lines, which corresponds to the G2 population. Through this process, we obtained the RGB populational number ratio of $n(G1):n(G2) = 63:37 (\pm 3)$, which is in excellent agreement with that by Milone et al. (2017), who obtained $N_{\text{TypeII}}/N_{\text{TOT}} = 0.403 \pm 0.021$, where our G2 corresponds to the Type II classified by Milone et al. (2017).

It is worth noting the absence of any clear subpopulational $\|cn_{JWL}$ separations in the G1 (dark green) and G2 (purple) in M22, as shown in Figure 2(b), which is in sharp contrast to the normal GCs without metallicity spread (e.g. M3, M5, NGC 6723, and NGC 6752) exhibiting discrete double cn_{JWL} or $\|cn_{JWL}$ RGB sequences in our previous studies (e.g., see Lee 2017, 2018, 2019a,b). Instead, the G1 and G2 distributions projected onto the Δ_2 axis with the slope of -1 (i.e., on the line along the CN–CH anticorrelation) exhibit the double and triple peaks, respectively. Using multiple Gaussian decompositions, we obtained the subpopulational number ratios of $n(\text{CN-w}):n(\text{CN-s}) = 51:49 (\pm 4)$ for the G1 group and $n(\text{CN-w}):n(\text{CN-i}):n(\text{CN-s}) = 24:32:44 (\pm 5)$ for the G2 group, and we show our results in Figure 2(e)–(f). For G2 subpopulations, we performed Welch’s two sample t -tests to see if they are drawn from the same population and we show p -values in Table 3, suggesting that they are different subpopulations. In the G1 group, the fraction of the CN-w, ≈ 0.50 , is rather large compared to those of normal GCs with inter-

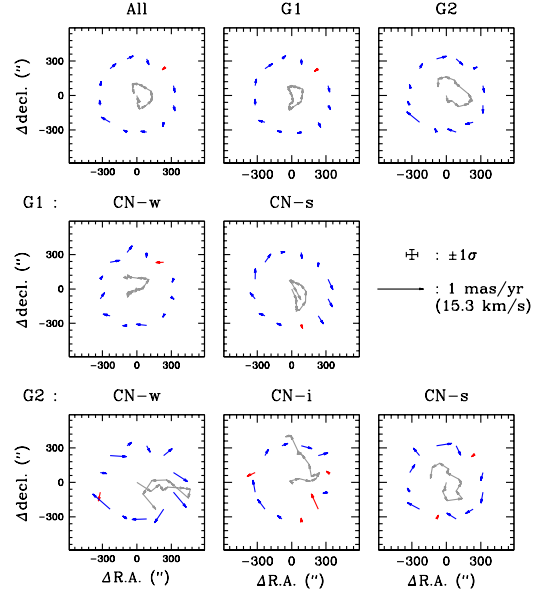


Figure 3. Distributions of the mean proper motions of 12 slices in the radial zone of $0.5 \leq r < 10'$. The red color denotes a clockwise rotation (E \rightarrow N \rightarrow W \rightarrow S \rightarrow E), while the blue color denotes a counterclockwise rotation at a given position vector. The gray arrows show evolutions of tangential vectors of consecutive slices in a counterclockwise sense starting at East. The G2 appears to have larger projected tangential velocities than the G1 does.

mediate to high total masses, ≈ 0.30 (e.g., see Lee 2017, 2018, 2019a,b; Milone et al. 2017). We note that the populational characteristic of the M22 G1 group (the subpopulational number ratio and the CRDs with a strong radial gradient as will be discussed below) is very similar to that of M3 (Lee 2019a).

3.3. Internal Rotation

We explore the internal rotation of individual subpopulations based on the proper motion study of the *Gaia* DR2 (Brown et al. 2018). We divided the sphere into 12 different slices in a single radial zone of $0.5 \leq r < 10'$. Then, we calculated the mean proper motion vectors in each slice and show our results in Figure 3. In the figure, we also show evolutions of tangential vectors of consecutive slices in a counterclockwise sense starting at east, where the size of the shape may indicate the degree of the internal rotation, although, for example, the G2 CN-i does not show a closed loop. Our results show that M22 has a substantial internal rotation (see also Sollima et al. 2019). We estimated rotational velocities of $1.9 \pm 0.1 \text{ km s}^{-1}$ and $2.4 \pm 0.4 \text{ km s}^{-1}$ for the G1 and G2, respectively, indicating that the G2 appears to have a slightly greater degree of internal rotation than the G1, consistent with our previous results from the radial velocity measurements (Lee 2015).

3.4. Cumulative Radial Distributions

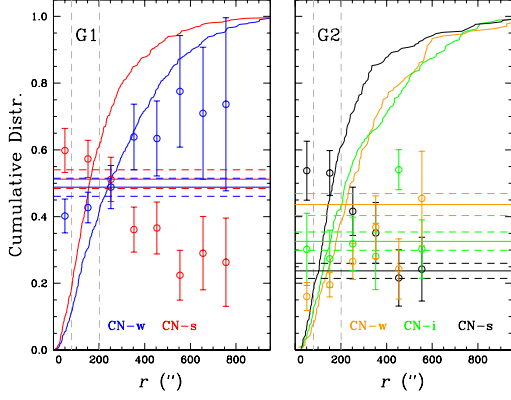


Figure 4. (Left) CRDs of the CN-w (blue) and CN-s (red) in the G1 group. The G1 CN-s is more centrally concentrated with a strong radial gradient. The vertical gray dashed lines denote the core and the half-light radii of the cluster. The horizontal solid lines denote the mean fractions of individual subpopulations, while the horizontal dashed lines the 1σ error of the mean. (Right) The CRDs of the CN-w (orange), CN-i (green), and CN-s (black) in the G2 group. Again, the G2 CN-s is more centrally concentrated with a strong radial gradient.

Table 4. K-S Tests for Cumulative Radial Distributions¹

Populations		p -value (%)	D
G1	vs. G2	29.2	0.052
G2(CN-w)	vs. G2(CN-i)	32.6	0.101
G2(CN-w)	vs. G2(CN-i + CN-s)	0.2	0.181
G1(CN-w)	vs. G2(CN-w)	61.5	0.072
G1(CN-w)	vs. G2(CN-i)	59.0	0.066
G1(CN-s)	vs. G2(CN-s)	62.4	0.058
G1(CN-w)	vs. G2(CN-w + CN-i)	85.7	0.043
G1(CN-s)	vs. G2(CN-i + CN-s)	4.2	0.091

¹ Inter-subpopulational comparisons with the p -value of 0.0% are omitted.

The CRDs of individual populations in GCs may provide a crucial information on the long-term dynamical evolution of GCs (e.g., see [Vesperini et al. 2013](#)). For normal GCs without any perceptible metallicity spread, the CRDs of the CN-w and CN-s populations in M5, NGC 6723, and NGC 6752 are very similar and statistical tests suggest that their CN-w and CN-s populations are most likely drawn from same parent distributions ([Lee 2017, 2018, 2019b](#)). On the other hand, the CN-s population in M3 shows a more centrally concentrated CRD ([Lee 2019a](#)).

Here, we derived the CRDs of individual subpopulations in M22 based on our photometric CN and CH abundances, and we obtained very intriguing results. First, the CRDs of the

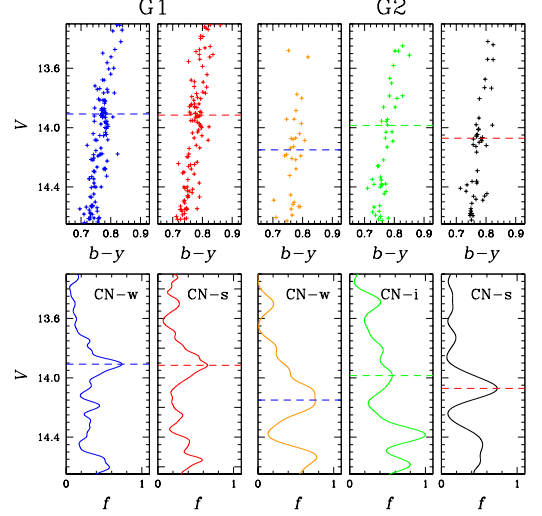


Figure 5. (Top panels) CMDs around the RGBB region. The horizontal dashed lines denote the RGBB V magnitude. (Bottom panels) Generalized differential luminosity functions.

Table 5. RGB Bump magnitudes

Populations		V
G1	CN-w	13.908 (± 0.025)
G1	CN-s	13.915 (± 0.025)
G2	CN-w	14.150 (± 0.040)
G2	CN-i	13.985 (± 0.040)
G2	CN-s	14.071 (± 0.040)

G1 and G2 groups are similar. We performed Kolmogorov–Smirnov (K-S) tests to derive the significance level for the null hypothesis that both distributions are drawn from the same distribution. We show the results for various cases in Table 4. Our K-S tests show that the G1 and G2 are most likely drawn from the same parent distribution with a p -value of 29.2%. Secondly, the CN-s subpopulations in both the G1 and G2 groups are more centrally concentrated with a strong radial gradient as shown in Figure 4, which is a very distinctive feature of M3 compared to other normal GCs ([Lee 2019a](#)). Finally, the CRD of the G1 CN-w is very similar to those of the G2 CN-w and CN-i, while the CRD of the G1 CN-s is very similar to that of the G2 CN-s.

3.5. Red Giant Branch Bump Magnitudes

During the evolution of the low-mass stars, the RGB stars experience slower evolution and temporary drop in luminosity when the very thin H-burning shell crosses the discontinuity in the chemical composition and lowered mean molecular weight left by the deepest penetration of the convective enve-

lope during the ascent of the RGB, the so-called RGB bump (RGBB; e.g., see [Cassisi & Salaris 2013](#)). The RGBB luminosity increases with helium abundance and decreases with metallicity at a given age.

We compared the RGBB V magnitudes in order to understand the relative metallicity and helium abundance between individual subpopulations. Figure 5 and Table 5 show our results. The G1 CN-w and CN-s have almost the same RGBB V magnitudes,² a strong observational line of evidence that both subpopulations have the same metallicity and helium abundance, in sharp contrast to normal GCs, such as M5, NGC 6723, and NGC 6752, with discernible helium enhancements in their CN-s populations ([Lee 2017, 2018, 2019b](#)). Our result poses a strong constraint on the polluter of the chemical evolution of the G1 group: no helium enhancement but variations in C and N. Furthermore, the extent of the C and N variations in the G1 group is smaller than that in the G2 group.

The RGBB of the G2 CN-w is 0.242 ± 0.047 mag fainter than the the G1 group, which can be translated into the metallicity difference of $\Delta[\text{Fe}/\text{H}] \approx 0.26 \pm 0.05$ dex³ if there was no helium enhancement, in the sense that the G2 CN-w is more metal rich than the G1. Our photometric estimate of metallicity difference is slightly larger than that of [Marino et al. \(2011\)](#), who obtained the metallicity difference between the two groups of stars in M22, $\Delta[\text{Fe}/\text{H}] \approx 0.15 \pm 0.02$ dex, by employing high-resolution spectroscopy. On the other hand, [Lee \(2016\)](#) employed the line-by-line differential spectroscopic analysis, obtaining $\Delta[\text{Fe}/\text{H}]_{\text{I}} = 0.20 \pm 0.04$ dex and $\Delta[\text{Fe}/\text{H}]_{\text{II}} = 0.17 \pm 0.06$ dex, in good agreement with that from RGBB V magnitudes.

Under the assumption that the whole stars in the G2 group have the same metallicity, which is reasonable because they have comparable hk_{JWL} strengths at a given V magnitude, the bright RGBB magnitudes in the G2 CN-i and CN-s can be interpreted that they are enhanced in helium by $\Delta Y \approx 0.03 - 0.07$ (± 0.02)⁴ with respect to the G2 CN-w, which is marginally in agreement with the population synthesis model of M22 by [Joo & Lee \(2013\)](#), who suggested a helium enhancement of $\Delta Y = 0.09$. It also should be mentioned that the fraction of the helium-enhanced population to explain the extreme blue horizontal branch (EBHB) population of M22

² Note that the G1 CN-w and CN-s have very similar hk_{JWL} strengths at a given V magnitude and, therefore, they have very similar metallicity. On the other hand, at a given V magnitude, the G2 group has a larger hk_{JWL} value than the G1 and, therefore, the G2 is more metal rich ([Lee 2015, 2016](#)).

³ In our previous work ([Lee 2015](#)), we derived a relation between the RGBB magnitude versus metallicity using results by [Bjork & Chaboyer \(2006\)](#), finding $\Delta M_{V,\text{bump}}/\Delta[\text{Fe}/\text{H}] \approx 0.93$ mag/dex.

⁴ We also derived a relation between RGBB magnitude and helium abundance using the results by [Valcarce, Catelan & Swigart \(2012\)](#), finding $\Delta m_{\text{bol}} \approx 2.5 \times \Delta Y$ for $Z = 1.6 \times 10^{-3}$ (see [Lee 2015](#)).

by [Joo & Lee \(2013\)](#) was about 0.30, which is in good agreement with that of our helium-enhanced populations (i.e., the G2 CN-i and CN-s RGB stars, which eventually evolve into the EBHB phase), 0.28 ± 0.04 .

4. SUMMARY AND CONCLUSION

Our $\|cn_{\text{JWL}}$ versus $\|ch_{\text{JWL}}$ of M22 RGB stars shows discrete double CN-CH anticorrelations, which are due to metallicity difference between the two groups of stars as we already discussed in our previous work ([Lee 2015](#)). Our populational number ratio of $n(\text{G1}):n(\text{G2}) = 63:37$ (± 3) is in excellent agreement with that by [Milone et al. \(2017\)](#).

The Δ_2 distribution of the G1 (i.e., the lower-metallicity group) can be fitted best with a two-component model without a helium enhancement between the two subpopulations, namely, the G1 CN-w and CN-s, inferred from their RGBB magnitudes, which is in sharp contrast to normal GCs with significant helium enhancements between the CN-w and CN-s populations (e.g., see [Lee 2017, 2018, 2019b; Lagioia et al. 2018; Milone et al. 2018](#)). On the other hand, the Δ_2 distribution of the G2 (i.e., the higher-metallicity group) can be fitted best with three subpopulations, namely, the G2 CN-w, CN-i, and CN-s. The G2 appears to be more metal rich than the G1 by $\Delta[\text{Fe}/\text{H}] \approx 0.26 \pm 0.05$ dex. Unlike the G1 group, the G2 CN-i and CN-s appear to be enhanced in helium by $\Delta Y \approx 0.03 - 0.07$ (± 0.02) with respect to the G2 CN-w, a generic feature of normal GCs. The fraction of the G2 CN-i and CN-s, which are helium-enhanced subpopulations and will eventually evolve into the EBHB, is 0.28 ± 0.04 , in good agreement with that estimated by [Joo & Lee \(2013\)](#).

The proper motion study from the *Gaia* DR2 allows us to reveal the the kinematical differences, in the sense that the G2 appears to rotate faster than the G1, confirming our previous results from the radial velocity measurements ([Lee 2015](#)).

In both main groups, the CRDs of the CN-s subpopulations are more centrally concentrated than other subpopulations. Interestingly, the CRDs of the G1 CN-s and the G2 CN-s are very similar. Likewise, the G1 CN-w and the G2 CN-w and CN-i have almost identical CRDs.

In our previous study ([Lee 2015](#)), we suggested that M22 most likely formed via a merger of two GCs,⁵ based on the chemical, kinematical, and structural differences between the Ca-w (i.e., the G1 group of this study) and Ca-s (i.e. the G2 group) populations. It is believed that our results presented in this work also strongly support the idea of the merger scenario for M22. For example, the sequential formation scenario (e.g., in a formation sequence of G1 CN-w \rightarrow G1 CN-s \rightarrow G2 CN-w \rightarrow G2 CN-i \rightarrow G2 CN-s, in which the metallicity evolution from the G1 to G2 groups and the helium enhancements in the G2 CN-i and CN-s can be explained, or in

⁵ Recently, [Massari et al. \(2019\)](#) suggested that M22 is an in situ GC.

different sequences) cannot be reconciled with the kinematical properties and the CRDs of the subpopulations in the G1 and G2 groups. If so, the synchronization of the CRDs of the individual subpopulations between the G1 and G2 may hint that the CRDs of individual subpopulations in the G1 and G2 are mass-independent, but, perhaps, they are governed by some global processes. Future theoretical simulations based on new results of chemical, structural, and kinematical dif-

ferences between MSPs will help to reveal the true story of M22.

J.-W.L. acknowledges financial support from the Basic Science Research Programs (grant Nos. 2016-R1A2B4014741 and NRF-2019R1A2C2086290) through the National Research Foundation of Korea (NRF). He also thanks Donghoh Kim for a helpful discussion and the anonymous referee for a constructive review of the manuscript.

REFERENCES

- Bjork, S. R., & Chaboyer, B. 2006, *ApJ*, 64, 1102
- Brown, A. G. A., Vallenari, A., Prusti, T., et al. 2018, *A&A*, 616, A1
- Cassisi, S., & Salaris, M. 2013, *Old Stellar Populations: How to Study the Fossil Record of Galaxy Formation* (Berlin:Wiley-VCH)
- Hesser, J. E., & Harris, G. L. H. 1979, *ApJ*, 234, 513
- Joo, S.-J., & Lee, Y.-W. 2013, *ApJ*, 762, 36
- Lagioia, E. P., Milone, A. P., Marino, A. F., et al. 2018, *MNRAS*, 475, 4088
- Lee, J.-W. 2015, *ApJS*, 219, 7
- Lee, J.-W. 2016, *ApJS*, 226, 16
- Lee, J.-W. 2017, *ApJ*, 844, 77
- Lee, J.-W. 2018, *ApJS*, 238, 24
- Lee, J.-W. 2019a, *ApJ*, 872, 41
- Lee, J.-W. 2019b, *ApJ*, 883, 166
- Lee, J.-W., & Carney, B. W. 1999, *AJ*, 117, 2868
- Lee, J.-W., Carney, B. W., Fullton, L. K., & Stetson, P. B. 2001, *AJ*, 122, 3136
- Lee, J.-W., Kang, Y.-W., Lee, J., & Lee, Y.-W. 2009a, *Nature*, 462, 480
- Lee, J.-W., & Pogge, R. 2016, *JKAS*, 49, 289
- Lim, D. et al. 2015, *ApJS*, 216, 19
- Marino, A. F., Milone, A. P., Piotto, G., et al. 2009, *A&A*, 505, 1099
- Marino, A. F., Sneden, C., Kraft, R. P., et al. 2011, *A&A*, 532, A8
- Massari, D., Koppelman, H. H., & Helmi, A. 2019, *A&A*, 630, L4
- Milone, A. P., Marino, A. F., Mastrobuono-Battisti, A., & Lagioia, E. P. 2018, *MNRAS*, 479, 5005
- Milone, A. P., Piotto, G., Renzini, A., et al. 2017, *MNRAS*, 464, 3636
- Muciarelli, A., Lapenna, E., Massari, D., et al. 2015, *ApJ*, 808, 128
- Norris, J., & Freeman, K. C. 1983, *ApJ*, 266, 130
- Sollima, A., Baumgardt, H., & Hilker, M. 2019, *MNRAS*, 485, 1460
- Stetson P. B. 1987, *PASP*, 99, 191
- Stetson P. B. 1994, *PASP*, 106, 250
- Valcarce, A., Catelan, M., & Sweigart, A. 2012, *A&A*, 547, A5
- Vesperini, E., McMillan, S. L. W., D'Antona, F., & D'Ercole, A. 2013, *MNRAS*, 429, 1913
- Zacharias, N., Monet, D. G., Levine, S. E., et al. 2004, *AAS*, 205, 4815